ACS Partner Journal

CHEMICAL & BIOMEDICAL IMAGING

Open Access

pubs.acs.org/ChemBioImaging

Article

Dual-Emission Fluorescent Probe for Simultaneous Visualization of Monoamine Oxidase A and Lysyl Oxidase in Alzheimer's Disease Cell Models

Yanyan Chen, Xiuxiu Wang, Wei Wei,* Ling Zhang,* Jing Zhao,* and Yong Qian*

Cite This: https://doi.org/10.1021/cbmi.5c00102

Read Online

ACCESS | Metrics & More | Article Recommendations | Supporting Information

ABSTRACT: Monoamine oxidase A (MAO-A) and lysyl oxidase (LOX) are two distinct amine oxidases that play crucial roles in many neurodegenerative diseases. Despite their similar enzymatic nature, their spatial distribution in different diseases and potential synergistic effects are poorly understood, partly due to the technical difficulties in detecting them concurrently. Herein, we designed and synthesized a series of dicyanoisophorone-based fluorescent probes, **MAP-X** (X = 2F, 2Cl, 2Br, F, Cl, Br), among which **MAP-2F** exhibits dual-emission fluorescence with high selectivity, enabling real-time visualization and simultaneous imaging of MAO-A (660 nm) and LOX (530 nm) in neuronal cells. By conducting experiments on neuronal cell models of Alzheimer's disease (AD) treated with Aβ_{42} oligomers, aggregates, and glutamate, the probe successfully detected dynamic changes in MAO-A and LOX. Further screening of 20 AD-related natural products revealed that several of them exhibited significant inhibitory effects on MAO-A and LOX, and were associated with the production, clearance, or activity of Aβ protein. These results indicate a close relationship between the expression of MAO-A and LOX and changes in Aβ protein levels. The simultaneous detection of MAO-A and LOX in AD-model cells provides an approach for studying the pathological mechanisms of AD and developing potential therapeutic targets.

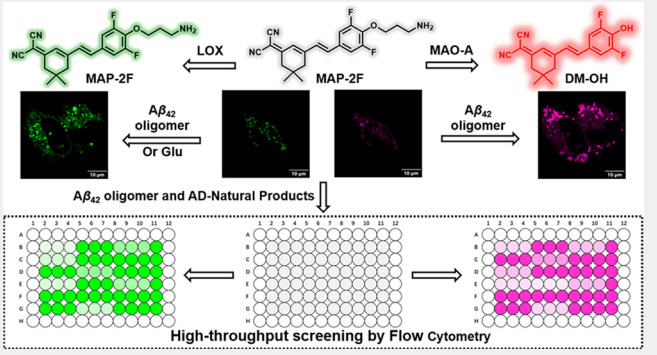

KEYWORDS: *monoamine oxidase A, lysyl oxidase, dual-emission fluorescent probe, Alzheimer's disease, high-throughput screening*

INTRODUCTION

Monoamine oxidases (MAOs) are flavin-dependent enzymes that catalyze the oxidative deamination of primary, secondary, and tertiary amines to produce the corresponding imines, which are then hydrolyzed to aldehydes. In humans, two isoenzymes have been identified, MAO-A and MAO-B, which share approximately 73% homology in sequence but are encoded by two different genes and have distinct tissue allocation systems and separate substrate specificities.[1,2] MAO-A preferentially metabolizes larger intrinsic amines, such as epinephrine, serotonin, and norepinephrine, whereas MAO-B has a higher affinity for β-phenylethylamine and benzylamine. Both isoforms are capable of oxidizing tyramine and dopamine.[3−7] Based on this, monoamine oxidase plays a key role in regulating neurotransmitter homeostasis in the nervous system, and abnormalities in its activity have been associated with the progression of a variety of neurodegenerative diseases, including AD.[8−17] Therefore, the development of fluorescence detection techniques that can specifically distinguish MAO-A from MAO-B is of great significance for dissecting their respective contributions to disease and designing isoform-selective therapeutic strategies.

Lysyl oxidase (LOX), a copper-dependent amine oxidase, represents a structurally and functionally distinct member of the amine oxidase family.[18−22] Unlike the intracellular localization of MAOs, LOX primarily operates in the extracellular matrix (ECM), where it catalyzes the oxidative deamination of lysine residues in collagen and elastin, facilitating their cross-linking and contributing to ECM structural integrity.[23−25] Abnormalities in LOX expression or activity have been associated with a variety of pathologies, including neurodegenerative diseases.[26−36] However, the current methods for real-time monitoring of LOX activity in complex biological systems remain limited, particularly in the context of AD.[37−40] Notably, despite differences in catalytic substrates and cellular localization of LOX and MAO-A/B, emerging evidence suggests that they may share commonalities

Received: July 9, 2025
Revised: August 2, 2025
Accepted: August 12, 2025

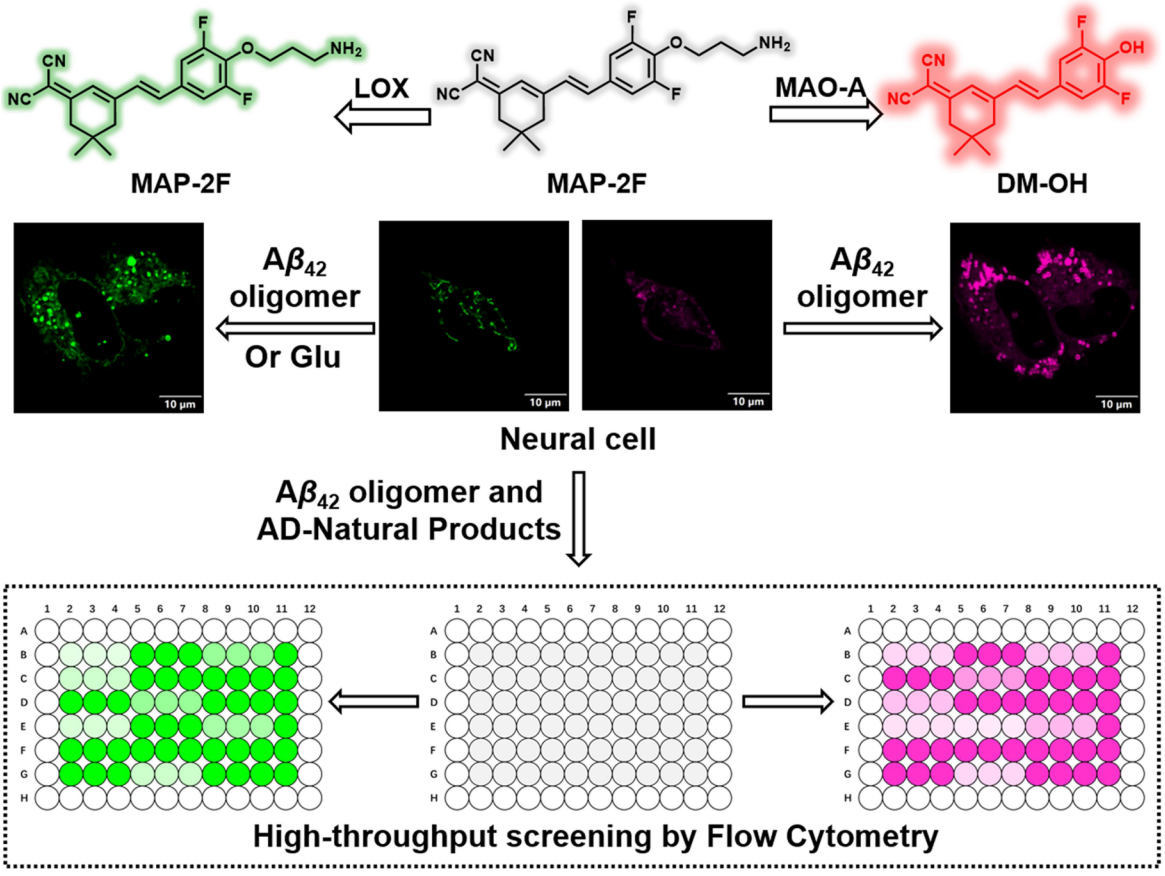

Figure 1. Schematic illustration of the detection mechanism and biological application of the dual-responsive fluorescent probe **MAP-2F** for the simultaneous detection of LOX and MAO-A.

in contributing to AD pathology; MAO-A/B is associated with oxidative stress and neurotransmitter dysregulation, whereas LOX may influence amyloid plaque formation and ECM remodeling, both of which are hallmarks of AD progression. Thus, the ability to monitor both enzymes simultaneously in biological systems may provide valuable mechanistic insights into their interactions and roles in neurodegenerative pathologies.

Here, we report the development of a series of near-infrared (NIR) fluorescent probes, **MAP-X** (X = 2F, 2Cl, 2Br, F, Cl, Br), based on dicyanoisophorone and propylamine scaffolds. We achieved selectivity by employing rational halogen substitutions to modulate the reactivity of the probes with the enzyme. Among them, **MAP-2F** exhibited selective and rapid detection of MAO (λ_{em} = 660 nm and LOD = 83.38 ng/mL) under 488 nm excitation. Remarkably, the same probe also enabled the detection of LOX at a distinct emission wavelength (λ_{em} = 530 nm), with a spectral separation of ∼130 nm, effectively minimizing crosstalk, and facilitated the realization of simultaneous monitoring of the two enzymes. Cellular imaging experiments confirmed the probe's ability to simultaneously visualize endogenous MAO-A and LOX activity in live neuronal cells. In AD cellular models induced by $A\beta_{42}$ oligomers and glutamate, **MAP-2F** successfully tracked changes in enzyme activity. Moreover, screening of 20 natural products associated with AD revealed several candidates with dual-inhibitory effects on MAO-A and LOX, implicating them in the regulation of AD pathology (Figure 1). Collectively, this work introduces a powerful chemical tool for the simultaneous imaging of MAO-A and LOX in neurodegenerative disease models and offers a new strategy for investigating their cooperative roles in AD pathogenesis and therapeutic development.

EXPERIMENTAL SECTION

Reagents and Instruments

The reagents and instruments employed in this study are detailed in the Supporting Information.

Synthesis of Probe MAP-X

A solution of **DM-X-NBoc** (1 equiv) in 5 mL of a mixed solvent of dichloromethane (DCM) and methanol (MeOH) (DCM/MeOH = 5/1) containing 4 M HCl was stirred at room temperature for 2 h. Upon completion, the reaction mixture was quenched and neutralized by the addition of saturated $NaHCO_3$, and then it was extracted with ethyl acetate. The organic phase was collected and dried with anhydrous magnesium sulfate. Finally, the solvent was evaporated, and the crude product was purified by silica gel column chromatography to afford the target compound **MAP-X** as an orange or yellow solid.

MAP-2F. 0.1 mmol, 28.9 mg, 75.3%, ^{1}H NMR (400 MHz, DMSO-d_6, 298 K) δ 8.04 (s, 3H), 7.55 (d, J = 9.7 Hz, 1H), 7.30 (m, 3H), 6.90 (s, 1H), 4.25 (t, J = 6.1 Hz, 2H), 2.96 (m, 2H), 2.63 (s, 2H), 2.51 (s, 2H), 2.01 (m, 2H), 1.02 (s, 6H); ^{13}C NMR (100 MHz, DMSO-d_6, 298 K) δ 170.20, 156.39, 154.95, 153.95,134.61, 132.02, 131.08, 123.55, 116.52, 113.66, 112.89, 111.71, 111.47, 77.17, 71.52, 42.18, 38.08, 35.83, 31.65, 27.58, 27.39; HRMS: calculated to be $[M + H]^+$ 384.1882, found: 384.1871.

MAP-2Cl. 0.1 mmol, 32.1 mg, 77.0%, ^{1}H NMR (400 MHz, DMSO-d_6, 298 K) δ 7.88 (s, 2H), 7.83 (s, 3H), 7.37 (m, 2H), 6.93 (s, 1H), 4.10 (t, J = 6.1 Hz, 2H), 3.07 (q, 2H), 2.63 (s, 2H), 2.51 (s,

https://doi.org/10.1021/cbmi.5c00102
Chem. Biomed. Imaging XXXX, XXX, XXX−XXX

2H), 2.07 (m, 2H), 1.01 (s, 6H); ^{13}C NMR (100 MHz, DMSO-d_6, 298 K) δ 170.68, 155.39, 151.12, 134.92, 134.26. 132.14, 129.30, 128.58, 124.30, 114.13, 113.34, 77.87, 71.47, 42.68, 38.56, 36.83, 32.14, 28.26, 27.90; HRMS: calculated to be $[M + H]^+$ 416.1291, found: 416.1278.

MAP-2Br. 0.1 mmol, 41.1 mg, 81.2%, ^{1}H NMR (400 MHz, DMSO-d_6, 298 K) δ 8.06 (s, 2H), 7.91 (s, 3H), 7.37 (m, 2H), 6.93 (s, 1H), 4.06 (t, J = 6.1 Hz, 2H), 3.06 (m, 2H), 2.63 (s, 2H), 2.49 (s, 2H), 2.11 (m, 2H), 1.01 (s, 6H); ^{13}C NMR (100 MHz, DMSO-d_6, 298 K) δ 170.71, 155.50, 152.97, 136.02, 134.32, 132.21, 132.09, 124.24, 118.63, 114.15, 113.34, 77.78, 71.23, 42.69, 38.56, 36.76, 32.12, 28.18, 27.91; HRMS: calculated to be $[M + H]^+$ 506.0261, found: 506.0254.

MAP-F. 0.1 mmol, 25.2 mg, 69.3%, ^{1}H NMR (400 MHz, DMSO-d_6, 298 K) δ 8.04 (s, 3H), 7.69 (dd, J = 12.9, 1.9 Hz, 1H), 7.47 (d, J = 9.2 Hz, 1H), 7.27 (m, 3H), 6.89 (s, 1H), 4.20 (t, J = 6.1 Hz, 2H), 2.95 (m, 2H), 2.62 (s, 2H), 2.52 (s, 2H), 2.06 (m, 2H), 1.02 (s, 6H); ^{13}C NMR (100 MHz, DMSO-d_6, 298 K) δ 170.29, 155.87, 152.92, 147.39, 136.36, 128.76, 125.57, 122.46, 114.83, 114.31, 114.12, 113.88, 113.08, 76.00, 65.78, 42.24, 38.12, 35.95, 31.66, 27.41, 26.65; HRMS: calculated to be $[M + H]^+$ 366.1977, found: 366.1966.

MAP-Cl. 0.1 mmol, 33.4 mg, 87.6%, ^{1}H NMR (400 MHz, DMSO-d_6, 298 K) δ 8.00 (s, 3H), 7.89 (d, J = 2.0 Hz, 1H), 7.64 (dd, J = 8.6, 1.9 Hz, 1H), 7.25 (m, 3H), 6.88 (s, 1H), 4.22 (t, J = 6.0 Hz, 2H), 2.98 (m, 2H), 2.62 (s, 2H), 2.52 (s, 2H), 2.07 (m, 2H), 1.02 (s, 6H); ^{13}C NMR (100 MHz, DMSO-d_6, 298 K) δ 170.79, 156.38, 154.92, 136.43, 130.46, 129.25, 129.15, 129.07, 123.02, 122.52, 114.43, 113.57, 76.54, 66.31, 42.75, 38.62, 36.57, 32.15, 27.92, 27.14; HRMS: calculated to be $[M + H]^+$ 382.1681, found: 382.1671.

MAP-Br. 0.1 mmol, 29.6 mg, 69.5%, ^{1}H NMR (400 MHz, DMSO-d_6, 298 K) δ 8.04 (d, J = 1.9 Hz, 1H), 7.92 (s, 3H), 7.68 (dd, J = 8.6, 1.9 Hz, 1H), 7.35 (m, 2H), 7.16 (d, J = 8.7 Hz, 1H), 6.88 (s, 1H), 4.21 (t, J = 6.0 Hz, 2H), 3.00 (m, 3H), 2.62 (s, 2H), 2.51 (s, 2H), 2.06 (m, 2H), 1.02 (s, 6H); ^{13}C NMR (100 MHz, DMSO-d_6, 298 K) δ 170.78, 156.40, 155.78, 136.34, 132.22, 130.95, 129.68, 129.20, 122.99, 114.38, 114.24, 113.57, 112.24, 76.50, 66.35, 42.75, 38.62, 36.60, 32.14, 27.93, 27.14; HRMS: calculated to be $[M + H]^+$ 426.1176, found: 426.1165.

Fluorescence Responses of MAP-X to Lysyl Oxidase (LOX) and Monoamine Oxidase (MAO)

First, we evaluated the time-dependent fluorescence response of **MAP-X** to LOX, **MAP-X** was incubated in borate buffer solution (BBS, 15 mM, pH 8.0, containing 20 μM Cu^{2+}) with or without LOX (50 μg/mL). The probe was added to a final concentration of 10 μM, and the reaction mixture was incubated at 37 °C under gentle rotation using a tube rotator. And the fluorescence emission spectra were recorded at various time points. Simultaneously, an analogous time-course experiment was conducted to assess the response of **MAP-X** to monoamine oxidase (MAO). In this case, the assay was performed in phosphate-buffered saline (PBS, 10 mM, pH 7.4), with or without MAO (20 μg/mL), under otherwise identical conditions.

To measure the fluorescence response of **MAP-2F** toward LOX, **MAP-2F** (10 μM) was incubated in BBS buffer (pH = 8.0) containing different concentration of LOX (0, 5, 10, 15, 20, 25, 30, 25, 40, 45, 50, 55, 60, 70, 80, 90, and 100 μg/mL) at 37 °C for 2 h.

Meanwhile, to measure the fluorescence response of **MAP-2F** to different concentrations of MAO, **MAP-2F** (10 μM) were incubated in PBS buffer (pH = 7.4) containing different concentration of MAO (0, 2.4, 4.8, 7.2, 9.6, 12, 14.4, 16.8, 18, 19.2, 20.4, 21.6, 22.8, 24, 25.2, 26.4, 27.6, and 28.8 μg/mL,) at 37 °C for 2 h.

A calibration curve was constructed by plotting the fluorescence intensity against the LOX/MAO concentration, and linear regression analysis was performed over the full concentration range. The slope (k) of the linear fit was then used to calculate the limit of detection (LOD) according to the following formula:

$$\text{limit of detection(LOD)} = 3\sigma/k$$

The standard deviation σ of the blank signal was again determined from 20 repeated measurements of **MAP-2F** in BBS (for LOX, σ = 17.63) and in PBS (for MAO, σ = 8.62) without an enzyme.

The LOD of **MAP-2F** for LOX was then determined to be 0.92 μg/mL. The detection limit of **MAP-2F** for MAO was then determined to be 83.38 ng/mL.

To assess the selectivity of **MAP-2F** toward different analyte, **MAP-2F** (10 μM) was incubated with various analytes, including metal ions (Pb^{2+}; Ce^{3+}; Mg^{2+}; Mn^{2+}; Zn^{2+}; Pd^{2+}; Co^{2+}; Cu^{2+}; Al^{3+}; Cr^{3+}), amino acids (L-Cys; L-Ala; L-Met; L-Tyr; L-Leu; L-Phe; L-Val; L-Ile; L-Pro; L-Lys), ROS/RNS (NO_2^-; HS^-; ClO^-; HO•; H_2O_2; $^1O_2$; TBHP), and human serum albumin (HSA), glutathione (GSH), Aβ_{42} aggregate, LOX, and MAO. Reactions were carried out in BBS for LOX and PBS for MAO at 37 °C for 2 h. Fluorescence spectra were subsequently recorded to evaluate the probe's response toward each analyte.

Cell Culture

Human neuroblastoma (SH-SY5Y) cells and human hepatocellular carcinoma (Hep G2) cells were obtained from the American Type Culture Collection (Manassas, VA). SH-SY5Y cells were cultured in minimum essential medium (MEM, Gibco, 24 mL) and Ham's F12 nutrient medium (F12, Gibco, 24 mL) supplemented with 5.6 mL of fetal bovine serum (Life Technologies, USA), nonessential amino acids (0.56 mL), and 100 U/mL penicillin/100 U/mL streptomycin. Cells were maintained and grown at 37 °C in a humidified atmosphere with a 5% CO_2 incubator. HepG2 cells were cultured in Dulbecco's modified Eagle's medium (DMEM, PAN Biotech, Germany) supplemented with 10% fetal bovine serum (Life Technologies, USA), sodium pyruvate, nonessential amino acids, and 100 U/mL penicillin/100 U/mL streptomycin. Cells were maintained and grown at 37 °C in a 5% CO_2 incubator.

Fluorescence Imaging Studies

Living SH-SY5Y and HepG2 cells were plated in confocal imaging dishes at a density of 80,000 cells/well and allowed to adhere overnight under standard culture conditions. Following incubation, the culture media were removed, and each well was washed with MEM/F12 medium (1:1, containing 10% FBS and 1% nonessential amino acids). Subsequently, 1000 μL of fresh media containing 10 μM **MAP-2F** was added to each well, and the cells were incubated at 37 °C in a humidified incubator with 5% CO_2 for 2 h. After incubation, the staining medium was removed and each well was washed three times with PBS before imaging.

To evaluate the effects of different aggregations of Aβ_{42} on the expression levels of MAO-A and LOX, SH-SY5Y cells were plated in confocal imaging dishes at a density of 80,000 cells/well and allowed to adhere for 12 h. The culture medium in each well was then replaced with 1000 μL of medium containing the various concentrations of Aβ_{42} monomer (0, 1, 2, and 5 μM), Aβ_{42} oligomer (0, 1, 2, and 5 μM), and Aβ_{42} aggregate (0, 1, 2, and 5 μM), followed by incubation at 37 °C in a humidified 5% CO_2 for 12 h. After treatment, the medium was removed and each well was washed with MEM/F12 medium (1:1, containing 10% FBS and 1% nonessential amino acids). Then, cells were incubated with 1000 μL of medium containing 10 μM **MAP-2F** for 2 h at 37 °C. After staining, the cells were washed three times with PBS before imaging.

In a parallel time-course study, SH-SY5Y cells were treated with an Aβ_{42} monomer, oligomer, or aggregate (each at 5 μM) for varying durations (2, 4, 6, and 8 h) under identical conditions. Following each time point, the staining and imaging procedures were performed as described above.

To investigate the impact of Glu-induced excitotoxicity on endogenous MAO-A and LOX activities, SH-SY5Y cells were plated in confocal imaging dishes at a density of 80,000 cells/well and allowed to adhere for 12 h. The culture medium in each well was then replaced with 1000 μL of fresh medium containing Glu (5 mM), and the cells were incubated at 37 °C in a humidified 5% CO_2 for different times (2, 4, 6, and 8 h). Following incubation, the medium was removed and each well was washed with MEM/F12 medium (1:1, containing 10% FBS and 1% nonessential amino acids). Cells were then treated with 1000 μL of medium containing 10 μM **MAP-2F** and

https://doi.org/10.1021/cbmi.5c00102
Chem. Biomed. Imaging XXXX, XXX, XXX−XXX

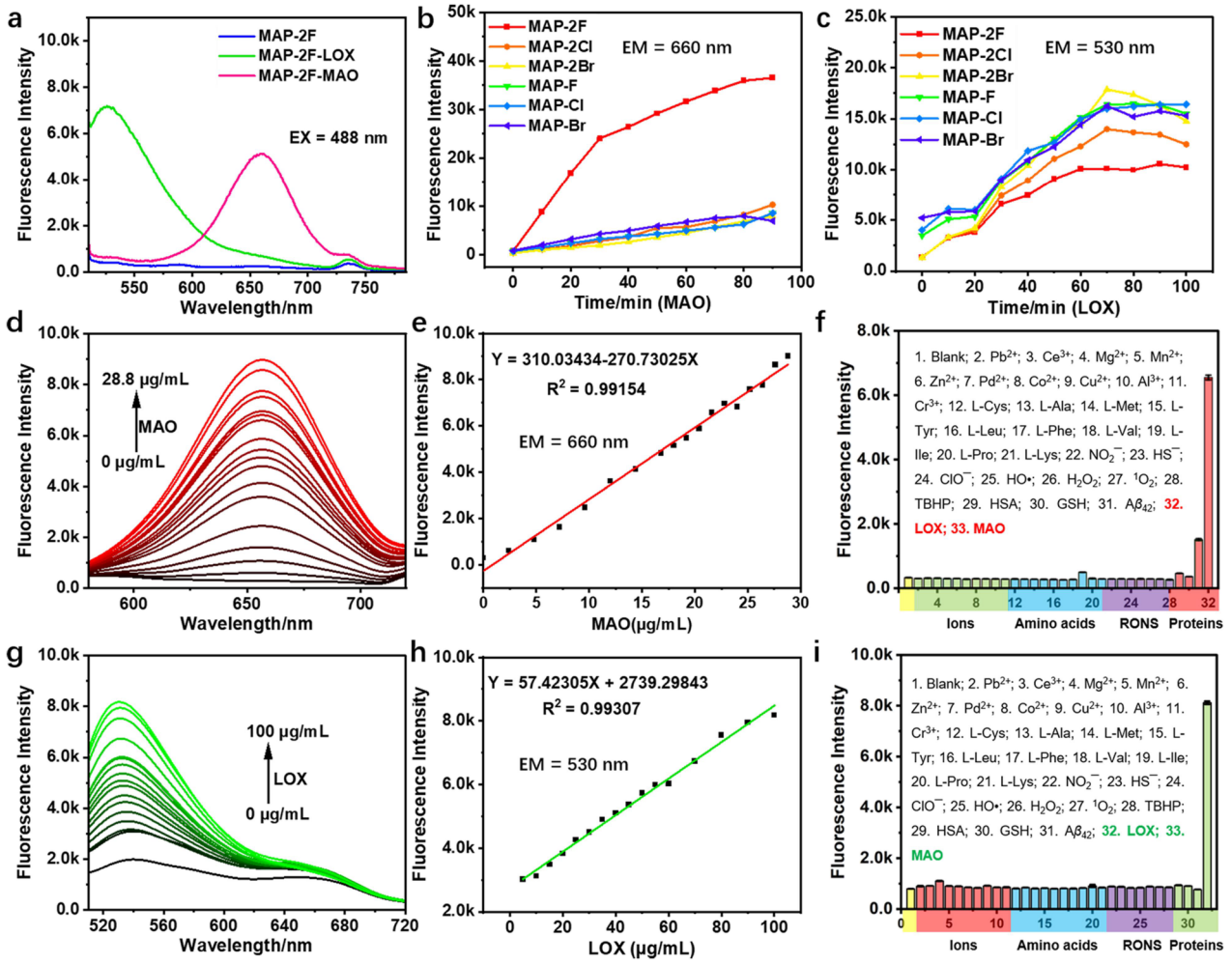

Figure 2. Spectroscopic characterization and selectivity of **MAP-2F** and **MAP-X** series toward MAO and LOX. (a) Fluorescence emission spectra of **MAP-2F** before and after incubation with MAO and LOX, showing distinct emission peaks at 660 and 530 nm, respectively. (b, c) Time-dependent fluorescence responses (0−100 min) of **MAP-X** toward MAO (b) and LOX (c) under physiological conditions. (d) Concentration-dependent fluorescence responses of **MAP-2F** toward MAO (0−28.8 μg/mL). (e) Linear calibration curve of **MAP-2F** fluorescence intensity versus MAO concentration. (f) Selectivity profile of **MAP-2F**, fluorescence intensity ratios in response to various biological analytes in PBS buffer. (g) Fluorescence intensity of **MAP-2F** upon exposure to increasing concentrations of LOX (0−100 μg/mL). (h) Linear fluorescence response of **MAP-2F** as a function of the LOX concentration. (i) Fluorescence intensity ratios of **MAP-2F** and **MAP-2F** toward various analytes in BBS buffer ($C_{\text{MAP-X}}$ = 10 μM, λ_{ex} = 488 nm, slit = 10/10 nm, 37 °C).

incubated for another 2 h. After staining, cells were rinsed three times with PBS before imaging.

To assess the specificity of **MAP-2F** for MAO-A and LOX, SH-SY5Y cells were seeded in confocal imaging dishes at a density of 40,000 cells/well and allowed to attach for 12 h. Cells were then pretreated with selective inhibitors in 500 μL of culture medium (β-aminopropionitrile (BAPN, 200 μM) and clorgyline (CL, 20 μM)) for 2 h. Following incubation, the medium was removed, and each well was washed with DMEM containing 10% FBS. Then, cells were incubated with 500 μL of medium containing 10 μM **MAP-2F** for 2 h under standard conditions. After staining, cells were rinsed thoroughly with PBS before imaging.

Screening of AD-Associated Natural Products by High-Content Analysis

SH-SY5Y cells were inoculated in 12-well plates at a density of 80,000/mL and allowed to adhere for 12 h. After incubation, cells were treated with 20 different AD-associated natural products: (1) coconut oil: CoOil; (2) ginkgo biloba leaf extract: Egb; (3) ursolic acid: UA; (4) stilbene glycoside; (5) caffeic acid; (6) resveratrol; (7) astragaloside IV; (8) *trans*-cinnamaldehyde; (9) icariin: ICA; (10) rhamnoside; (11) ginsenoside Rg1; (12) cornelian cherry; (13) teat polyphenols; (14) crocetin; (15) curcumin; (16) artemisinin; (17) kynurenine glycosides; (18) forsythiazide B; (19) tanshinone IIA; (20) tocopherol. All of the selected natural products were specifically chosen based on their well-documented roles in Alzheimer's disease pathology, including Aβ interactions (e.g., resveratrol for Aβ clearance, curcumin for Aβ aggregation inhibition); neuroprotective effects (e.g., tanshinone IIA for anti-inflammatory properties), etc. For compounds with defined molecular weights, a final concentration of 10 μM was used. For those without a known molecular weight (e.g., crude extracts), the working concentration was set at 10 μg/mL. Following compound treatment, cells were incubated for 12 h at 37 °C with 5% CO_2. The culture medium was then removed, and cells were washed three times with PBS. Then, cells were treated with the Aβ_{42} oligomer (5 μM) for an additional 12 h. After this incubation, the culture medium was removed, and the cells were treated with fresh medium containing 10 μM **MAP-2F** and then further incubated for 2 h. Finally, cells were washed three times with PBS to remove residual probe. Cells were then harvested by trypsinization, resuspended in PBS, and transferred to U-bottom 96-well plates for fluorescence quantification. High-content analysis was performed using flow cytometry on a NovoCyte Quanteon flow cytometer

https://doi.org/10.1021/cbmi.5c00102
Chem. Biomed. Imaging XXXX, XXX, XXX−XXX

(Agilent Technologies), with fluorescence signals collected in the FITC and PerCP channels to assess **MAP-2F** activation levels.

RESULTS AND DISCUSSION

Optical Response and Selectivity of MAP-X Probes toward MAO-A and LOX under Physiological Conditions

The synthetic route for the **MAP-X** series (**MAP-2F**, **MAP-2Cl**, **MAP-2Br**, **MAP-F**, **MAP-Cl**, and **MAP-Br**) is illustrated in Scheme S1, with full structural characterization provided in Figures S1−S42 (Supporting Information). To evaluate the enzyme-responsiveness of these **MAP-X** probes, we systematically investigated their optical properties under simulated physiological conditions. When incubated with MAO, only **MAP-2F** exhibited a significant fluorescence enhancement at 660 nm (Figure 2a), whereas the other probes (**MAP-2Cl, MAP-2Br, MAP-F**, **MAP-Cl**, and **MAP-Br**) showed minimal response (Figure S43b−f). In contrast, when exposed to LOX, all **MAP-X** probes demonstrated fluorescence activation at 530 nm, with no signal at 660 nm (Figure S43), suggesting a wavelength-resolved distinction between MAO-A and LOX responses. To further validate the superiority of **MAP-X** in detecting MAO and LOX, the fluorescence changes of **MAP-X** were examined when incubated with MAO and LOX at different times in phosphate buffer solution (PBS, pH = 7.4) and borate buffer solution (BBS, pH = 8.5), respectively. As shown in Figure 2b, an obvious fluorescence enhancement (I/I_0 = 31.34) was detected in the **MAP-2F** and MAO systems when incubated at 37 °C within 30 min. Under the same conditions, other probes (**MAP-2Cl**, **MAP-2Br**, **MAP-F**, **MAP-Cl**, and **MAP-Br**) showed only weak fluorescence changes even after 90 min of incubation, highlighting the unique reactivity of **MAP-2F** toward MAO. In contrast, incubation with LOX in BBS buffer led to a gradual increase in fluorescence at 530 nm for all probes (Figure 2c), with comparable response kinetics. This suggests that the LOX-induced fluorescence enhancement may be determined by noncovalent interactions (possibly driven by the affinity of the probes to the proteins) rather than by electronic effects of chemical uncaging. These data establish **MAP-2F** as a superior fluorogenic probe for MAO detection, while retaining competent responsiveness toward LOX. Notably, the emission maxima of **MAP-2F** upon activation of MAO and LOX differ by approximately 130 nm, which results in minimal spectral overlap for dual-channel imaging, an essential feature for the simultaneous detection of intracellular and extracellular amine oxidases.

To further assess the quantitative detection capabilities of **MAP-2F**, we performed concentration-dependent fluorescence assays. Upon exposure to increasing concentrations of MAO (0−30 μg/mL) in PBS, the emission intensity at 660 nm increased proportionally (Figure 2d), exhibiting an excellent linear relationship in the range of 0−0.03 μg/mL (Figure 2e). The limit of detection (LOD), calculated using the 3σ/slope method, was determined to be 83.38 ng/mL, suggesting ultrasensitive detection of MAO by **MAP-2F** *in vitro*. Similarly, incubation with LOX (0−100 μg/mL) led to concentration-dependent fluorescence enhancement at 530 nm (Figure 2g), with a strong linear relationship over the entire range (Figure 2h). The LOD for LOX was estimated to be 0.92 μg/mL. Importantly, no signal at 660 nm was observed in these experiments, which further confirmed the dual-analysis assay's feasibility.

Next, to assess the selectivity of **MAP-2F** for MAO and LOX in biologically relevant environments, we performed a fluorescence response analysis in the presence of a range of potential interferents. These included physiologically relevant metal ions, amino acids, reactive oxygen species (ROS), reactive nitrogen species (RNS), and common proteins. For MAO detection, **MAP-2F** (10 μM) was incubated in PBS buffer with each analyte individually at 37 °C for 1 h. As shown in Figure 2f, a substantial fluorescence enhancement at 660 nm was observed only in the presence of MAO (10 μg/mL), whereas other analytes did not induce significant signal changes. A slight increase in fluorescence was recorded in the presence of LOX, yet it remained significantly lower than that induced by MAO, highlighting the preferential response of the probe. To assess the specificity for LOX, similar experiments were performed in BBS buffer to monitor the emission at 530 nm. The test results revealed that only LOX triggered a pronounced fluorescence turn-on, while MAO and other interferents produced negligible responses (Figure 2i). This wavelength-resolved orthogonality strongly supports the dual-analyte discrimination capability of **MAP-2F**. Taken together, these findings confirm that **MAP-2F** exhibits high selectivity for MAO and LOX through different fluorescence channels (660 and 530 nm, respectively), with minimal cross-reactivity in complex environments. This dual-responsiveness highlights **MAP-2F** as a powerful molecular tool for real-time, selective imaging of both intra- and extracellular amine oxidase activity in living systems.

To further evaluate the potential imaging capacities of **MAP-2F** for MAO and LOX in living cells, we conducted a series of cellular assays. Initially, the cytotoxicity of **MAP-2F** was assessed in SH-SY5Y and Hep G2 cells using the MTT assay; the results indicated no significant decrease in cell viability upon treatment with **MAP-2F**, suggesting good biocompatibility for both cell types (Figure S44). To examine the selectivity of **MAP-2F** for MAO isoforms in living cells, we utilized the different expression profiles of MAO-A and MAO-B in SH-SY5Y and HepG2 cells.[41,42] As depicted in Figure S45, negligible fluorescence was observed in Hep G2 cells following **MAP-2F** treatment, implying minimal interaction with intracellular MAO-B. In contrast, SH-SY5Y cells exhibited strong fluorescence upon exposure to **MAP-2F**. This fluorescence signal was markedly diminished by preincubation with Clorgyline (CL), a selective MAO-A inhibitor,[43] while treatment with the MAO-B inhibitor Pargyline (PL)[44] had almost no effect. These findings robustly confirmed the selective ability of **MAP-2F** to recognize and respond to MAO-A in living cells. In addition, as summarized in Table S1, **MAP-2F** outperforms previously reported MAO-A and LOX probes in several key aspects, including faster response kinetics, higher sensitivity, and exceptional selectivity. Notably, **MAP-2F** uniquely enables the dual-analytical detection of MAO-A and LOX through distinct fluorescence emission channels. This superior dual-response capability provides a critical foundation for further applications in the synergistic monitoring of the dynamic interplay and potential coexpression patterns of MAO-A and LOX in complex biological contexts.

Elucidation of the Fluorescence Response Mechanism of MAP-2F to MAO and LOX

The distinct response mechanisms of **MAP-2F** toward MAO and LOX were investigated using ^{19}F nuclear magnetic

https://doi.org/10.1021/cbmi.5c00102
Chem. Biomed. Imaging XXXX, XXX, XXX−XXX

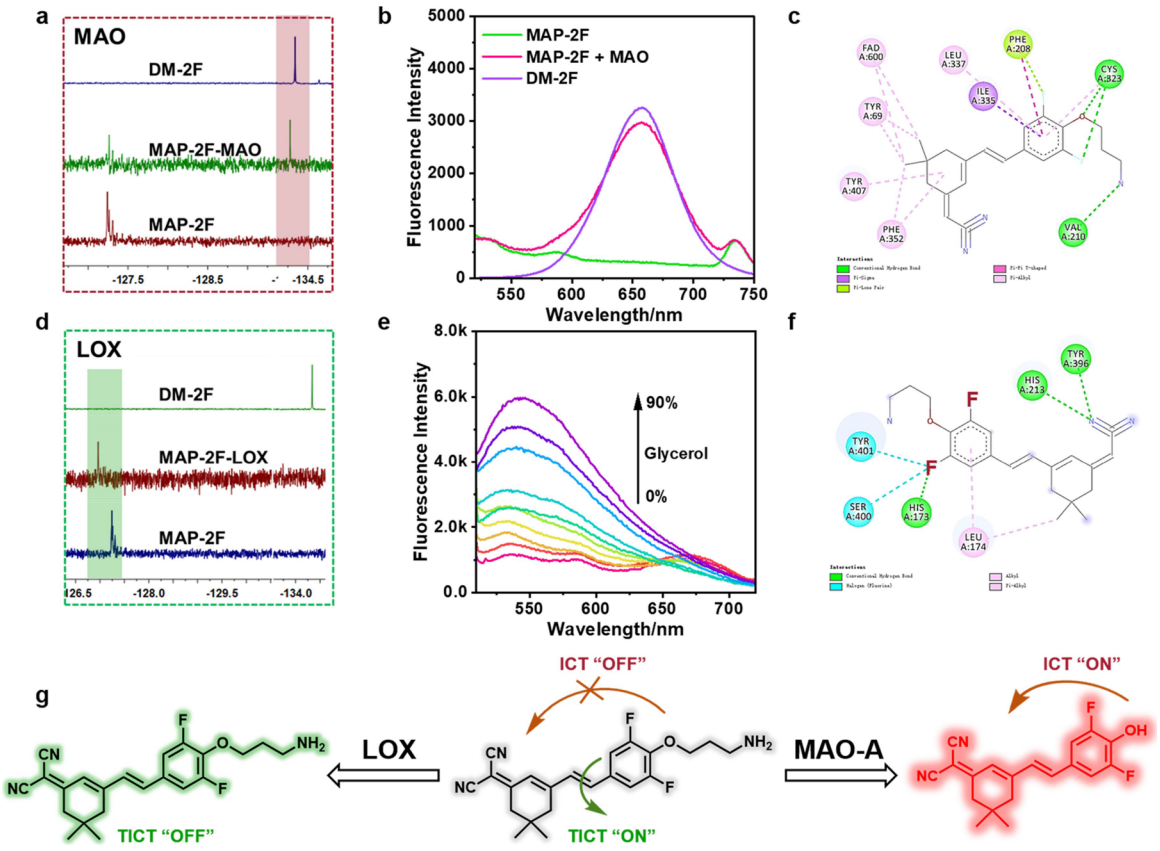

Figure 3. Mechanistic studies of the **MAP-2F** interactions with MAO and LOX. (a, d) The ^{19}F NMR spectra of **DM-2F**, **MAP-2F**, and **MAP-2F** after response to MAO (a) and LOX (d); (b) fluorescence emission spectra of **DM-2F**, **MAP-2F**, and **MAP-2F** after response to MAO. (c, f) Molecular docking simulations showed two-dimensional interaction maps between **MAP-2F** and MAO (c) or LOX (f), indicating distinct binding orientations and key amino acid interactions. (e) Fluorescence spectra of **MAP-2F** in various viscosity system (water/glycerol, v/v, $f_{glycerol}$ from 0 to 90%, λ_{ex} = 488 nm, slit = 10/10 nm). (g) Proposed enzymatic activation mechanisms of **MAP-2F** with MAO-A (left) and LOX (left), respectively.

resonance (^{19}F NMR) spectroscopy, which takes advantage of the unique 3,5-difluoro substitution of probe **MAP-2F**, and ^{19}F NMR analysis characterized by high sensitivity and minimal biological background. As shown in Figure 3a, the ^{19}F NMR signal of **MAP-2F** exhibited a chemical shift at −127.24 ppm. Upon incubation with MAO, a new signal appeared at −134.28 ppm, which was closely aligned to the chemical shift of the free fluorophore **DM-2F** (−134.34 ppm), indicating cleavage at the response site and subsequent release of the fluorophore. This cleavage event initiates an intramolecular charge transfer (ICT) process, thereby accounting for the observed fluorescence enhancement. Fluorescence emission measurements further supported these findings; the emission profile of **MAP-2F** upon reaction with MAO was consistent with that of **DM-2F** (Figure 3b), further confirming a fluorogenic reaction driven by enzymatic cleavage and fluorophore release. This mechanism is consistent with previous literature studies on MAO substrates, wherein oxidative deamination of the amine moiety generates an aldehyde intermediate that triggers β-elimination and fluorophore release.[45−47] In contrast, the ^{19}F NMR spectra of **MAP-2F** treated with LOX displayed a modest downfield shift of **MAP-2F** at −126.96 ppm without the appearance of new peaks (Figure 3d), suggesting a noncleavage mechanism. This observation indicates that the interaction between **MAP-2F** and LOX induces a restriction of intramolecular motion rather than a chemical transformation. To validate this hypothesis, we further examined the fluorescence emission in solvents of varying viscosity. The fluorescence intensity at 530 nm increased gradually with medium viscosity (Figure 3e), further suggesting that restricted molecular rotation of **MAP-2F**, potentially due to interaction with LOX, would obstruct the twisted intramolecular charge transfer (TICT) process and enhance fluorescence emission. Moreover, molecular docking analysis further confirmed these mechanistic differences. **MAP-2F** exhibited significantly stronger binding affinity toward LOX compared to MAO-A (Figures 3c, 3f, S46; Table S2), supporting the model wherein the LOX interaction stabilizes the molecular conformation of **MAP-2F**, restricts torsional freedom, and suppresses the TICT, thereby enhancing the fluorescence emission at 530 nm. In contrast, the MAO-A interaction facilitates the chemical transformation and release of **DM-2F**, producing a red-shifted emission centered at 660 nm. Taken all together, these results highlight that **MAP-2F** can distinguish between MAO-A and LOX, through a distinct response mechanism, a cleavage-induced ICT activation for MAO-A, and a conformationally restricted TICT suppression for LOX (Figure 3g). These mechanistic differences result in spectrally resolved fluorescence outputs, thereby minimizing spectral overlap for dual-channel imaging. This dual-response capability not only improves detection accuracy but also provides a rational reference for designing multianalyte fluorescent probes targeting structurally or functionally similar biomolecules in complex biological systems.

https://doi.org/10.1021/cbmi.5c00102
Chem. Biomed. Imaging XXXX, XXX, XXX−XXX

Dual-Channel Cellular Imaging of MAO-A and LOX under Aβ_{42} Exposure Stresses

Based on the extracellular fluorescence results indicating the dual-channel response of **MAP-2F** to MAO-A (660 nm) and LOX (530 nm), we further assessed the feasibility of using **MAP-2F** for simultaneous imaging of both enzymes in live cells. Confocal fluorescence imaging in SH-SY5Y cells, using excitation at 488 nm, revealed two distinct emission signals corresponding to green and red channels (Figure 4), which

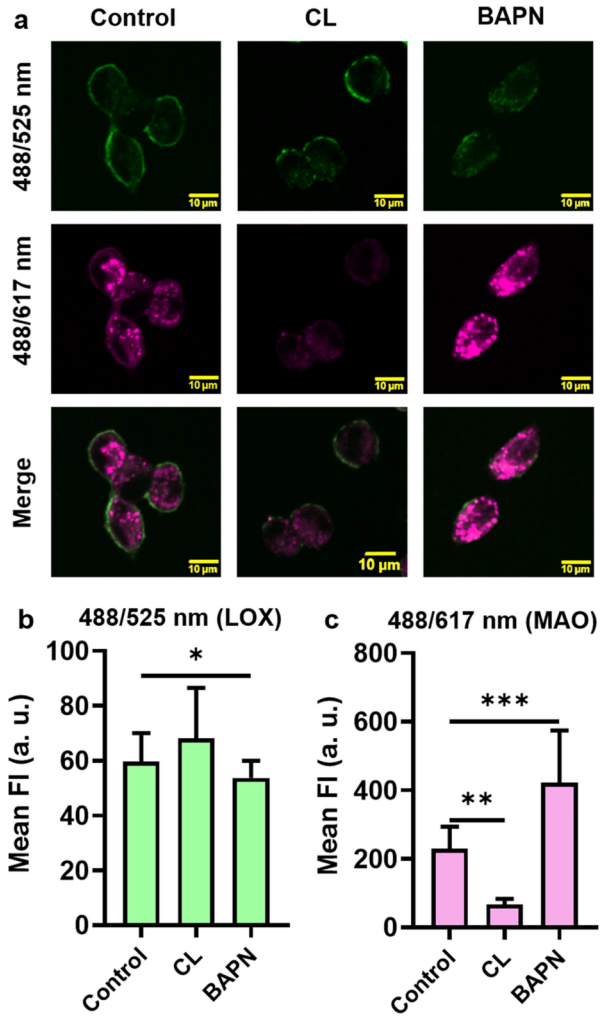

Figure 4. Fluorescence imaging of MAO-A and LOX activity in SH-SY5Y cells using **MAP-2F**. (a) Confocal fluorescence images of SH-SY5Y cells incubated with **MAP-2F** (10 μM), clorgyline (CL, 20 μM; MAO-A inhibitor), and β-aminopropionitrile (BAPN, 200 μM; LOX inhibitor). Dual-channel imaging reveals enzyme-specific signals: green channel (λ_{em} = 525 nm) for LOX and red channel (λ_{em} = 617 nm) for MAO-A. λ_{ex} = 488 nm, scale bars = 10 μm. (b, c) Quantification of mean fluorescence intensities from panel (a) in both emission channels. Data are presented as the mean ± standard deviation of three replicates. Multiple comparisons were performed by one-way ANOVA: *$P \leq 0.05$, **$P \leq 0.01$, and ***$P \leq 0.001$.

were consistent with the LOX- and MAO-A-mediated responses, respectively. Notably, pretreatment with clorgyline, a MAO-A inhibitor, significantly suppressed the red fluorescence signal in the red channel, confirming the specificity of **MAP-2F** for MAO-A in this spectral window. In contrast, β-aminopropionitrile (BAPN), a well-established LOX inhibitor,[48] exhibited only a minor inhibitory effect on green channel fluorescence. This result aligns with our proposed mechanism that **MAP-2F** interacts with LOX through noncatalytic nucleophilic binding rather than enzymatic oxidation and thus may not be completely inhibited by BAPN. Intriguingly, dual-channel imaging also revealed distinct subcellular localization patterns of the red and green signals, suggesting spatial segregation of MAO-A and LOX activity in the cellular environment. These findings collectively highlight that **MAP-2F** serves as an effective probe for dual-channel imaging of MAO-A and LOX activity dynamics in living neuronal cells, offering a valuable tool for elucidating the interactions between these two oxidative enzymes in complex biological systems.

Given the link between abnormal metabolism of MAO-A and LOX in neurodegeneration diseases, particularly in AD, and the central role of amyloid-β (Aβ_{42}) in the pathogenesis of AD,[11,13−17,13−17,37−40,49] we further explored whether **MAP-2F** could be used to monitor the impact of varying degrees of Aβ_{42} peptide on the activity dynamics of MAO-A and LOX in live neuronal cells. SH-SY5Y cells, previously validated as a suitable cell model for dual imaging with **MAP-2F**, were exposed to different concentrations of Aβ_{42} monomers, oligomers, and aggregates for 12 h, followed by incubation with **MAP-2F** for 2 h. As shown in Figure 5, a dose-dependent increase in fluorescence was observed in SH-SY5Y cells treated with Aβ_{42} oligomers and Aβ_{42} aggregates, whereas minimal fluorescence changes were observed in Aβ_{42} monomer-treated cells. These observations revealed that Aβ_{42} oligomers and aggregates significantly upregulate the intracellular levels and activities of MAO-A and LOX in live neuronal cells. To further investigate whether these effects on enzyme activity of MAO-A and LOX were time-dependent, SH-SY5Y cells were treated with Aβ_{42} monomers, oligomers, or Aβ_{42} aggregates for different times and then subjected to **MAP-2F** imaging (Figure S47). We found that the fluorescence signals of SH-SY5Y cells in the red and green channels increased significantly over time in the presence of Aβ_{42} oligomers and aggregates, further confirming the time- and dose-dependent upregulation of MAO-A and LOX under Aβ_{42} exposure stresses. Collectively, these findings reveal a clear correlation between Aβ_{42} oligomer-aggregate exposure stresses and the aberrant upregulation of MAO-A and LOX in live neuronal cells. The ability of **MAP-2F** to simultaneously visualize these enzymes in real-time and at distinct wavelengths makes it a powerful tool for dissecting the molecular mechanisms underlying AD pathology and potentially for evaluating therapeutic strategies targeting oxidative stress and enzyme dysregulation in neurodegenerative disorders.

Glutamate (Glu), an essential excitatory neurotransmitter in the brain, is known to exert neurotoxic effects and has been widely used in cellular models of AD *in vitro*. Based on studies that have shown an increase in LOX levels in neuronal cells after treatment with Glu,[35] a subsequent evaluation of the changes in MAO-A and LOX levels in SH-SY5Y neuronal cells post-Glu treatment was undertaken, as shown in Figure S48. The imaging findings indicated that the fluorescence intensity of the green channel, representing the LOX activity, increased in a time-dependent manner. In contrast, the fluorescence intensity of the red channel, representing MAO-A, increased relatively only slightly. These results demonstrate that Glu primarily upregulates LOX rather than MAO-A, thus emphasizing the critical role of LOX in Glu-induced

https://doi.org/10.1021/cbmi.5c00102
Chem. Biomed. Imaging XXXX, XXX, XXX−XXX

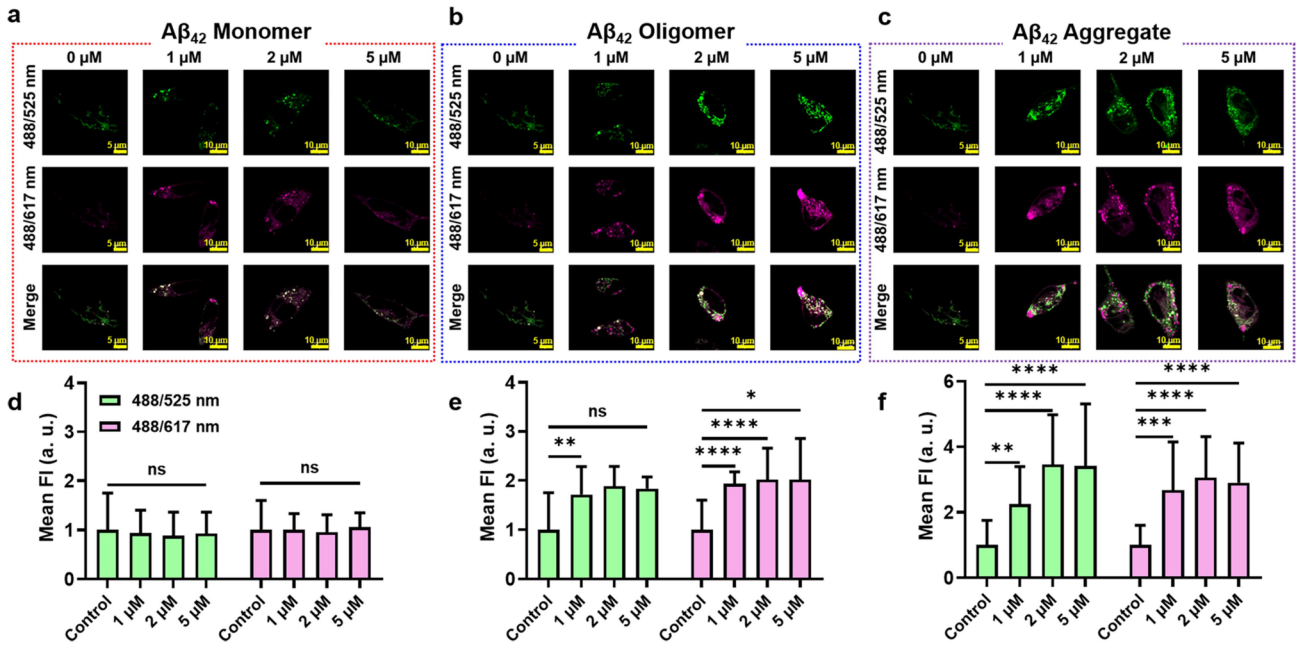

Figure 5. Fluorescence imaging of MAO-A and LOX activity in SH-SY5Y cells exposed to different Aβ_{42} species. (a–c) Confocal fluorescence images of SH-SY5Y cells treated with increasing concentrations of (a) Aβ_{42} monomers, (b) Aβ_{42} oligomers, and (c) Aβ_{42} aggregate for 12 h, followed by incubation with **MAP-2F** (10 μM) for 2 h (λ_{ex} = 488 nm; Green channel corresponds to LOX activity: 525 nm; red channel corresponds to MAO-A activity: 617 nm). (d–f) Quantification of mean fluorescence intensities from panels (a–c), respectively, revealing dose-dependent modulation of enzyme activity by different Aβ_{42} species. Data are shown as the mean ± standard deviation of three replicates. Statistical significance was assessed using one-way ANOVA with multiple comparisons: ns, $P > 0.05$; *$P \leq 0.05$; **$P \leq 0.01$; ***$P \leq 0.001$; ****$P \leq 0.0001$.

neurotoxicity and its potential contribution to AD pathophysiology. To validate these observations, we further performed a series of complementary experiments, including ELISA, Western blotting, and immunofluorescence assays (Figure S49). Consistently, the outcomes of these experiments all confirmed that the expression levels of both MAO-A and LOX were elevated in SH-SY5Y cells following treatment with AD-related factors such as Aβ_{42} oligomers, Aβ_{42} aggregates, and Glu. These results collectively support the notion that AD-related stimulus stresses promote differential yet simultaneous up-regulation of MAO-A and LOX in neuronal cells and further demonstrate the utility of **MAP-2F** in monitoring these concurrent changes in live AD-model cells. Furthermore, it has been established that overactivation of MAO-A contributes to the generation of Aβ monomers by facilitating β-and γ-secretase-mediated cleavage of amyloid precursor protein (APP), which ultimately leads to the formation of Aβ plaques.[50,51] Additionally, LOX has also been implicated in the cross-linking of extracellular matrix metabolism and aggregation of Aβ_{42} protein, thereby contributing to the pathology of AD.[37] These established roles prompted us to investigate a potential feedback mechanism wherein LOX facilitates the aggregation of Aβ_{42} monomers, potentially triggering further upregulation of MAO-A and LOX. To test this hypothesis, SH-SY5Y cells were exposed to Aβ_{42} oligomers or Glu for 4 h, followed by treatment with Aβ_{42} monomers for an additional 12 h. Subsequently, cells were treated with **MAP-2F** and subjected to fluorescence imaging (Figure S50a–f). The results demonstrated that the cotreatment resulted in a significant increase in fluorescence intensity in the green and red channels compared to the control groups with Glu or Aβ_{42} oligomers alone. These observations suggest that LOX, upregulated by Aβ_{42} oligomers or Glu, may facilitate the aggregation of intracellular Aβ_{42} monomers, which in turn stimulate MAO-A and LOX expression. Moreover, Western blot analysis confirmed this finding, showing elevated levels of MAO-A and LOX proteins in the cotreated cells compared to controls (Figure S50g–i). This observation further confirmed that the upregulation of MAO-A and LOX may be associated with the aggregation of Aβ_{42} monomers, thus supporting a self-reinforcing cyclical relationship between Aβ_{42} aggregation and the overexpression of MAO-A and LOX in neuronal cells.

High-Throughput Screening of MAO-A/LOX Regulators in the AD Cellular Model with MAP-2F

Finally, to further evaluate the efficacy of **MAP-2F** as a screening tool for potential MAO-A and LOX modulators in AD, we sought to combine **MAP-2F** staining with flow cytometry to develop a fluorescence-based high-throughput screening platform (Figure 6a). Living SH-SY5Y cells were first pretreated with various natural products possessing potential anti-AD properties for 12 h, followed by treatment with Aβ_{42} oligomers for 24 h, and subsequent **MAP-2F** staining. Flow cytometric analysis of the FITC (LOX) and PerCP (MAO-A) channels revealed distinct modulation patterns. Specifically, compounds such as ursolic acid, resveratrol, triptolide, corni fructus, forsythoside B, and stigmasterol significantly reduced LOX-associated fluorescence signal in the FITC channel (Figure 6b,c), suggesting effective suppression of LOX upregulation. Meanwhile, Icariin (ICA), curcumin, geniposidic acid, forsythoside B, tanshinone IIA, and stigmasterol markedly reduced the fluorescence of PerCP, suggesting that they inhibited the up-regulation of MAO-A (Figure 6d, e). Notably, forsythoside B and stigmasterol were the only compounds that effectively downregulated both MAO-A and LOX. Conversely, ursolic acid, Resveratrol, and Triptolide inhibited LOX activity while enhancing MAO-A fluorescence, a phenomenon previously observed following BAPN treatment, possibly

https://doi.org/10.1021/cbmi.5c00102
Chem. Biomed. Imaging XXXX, XXX, XXX–XXX

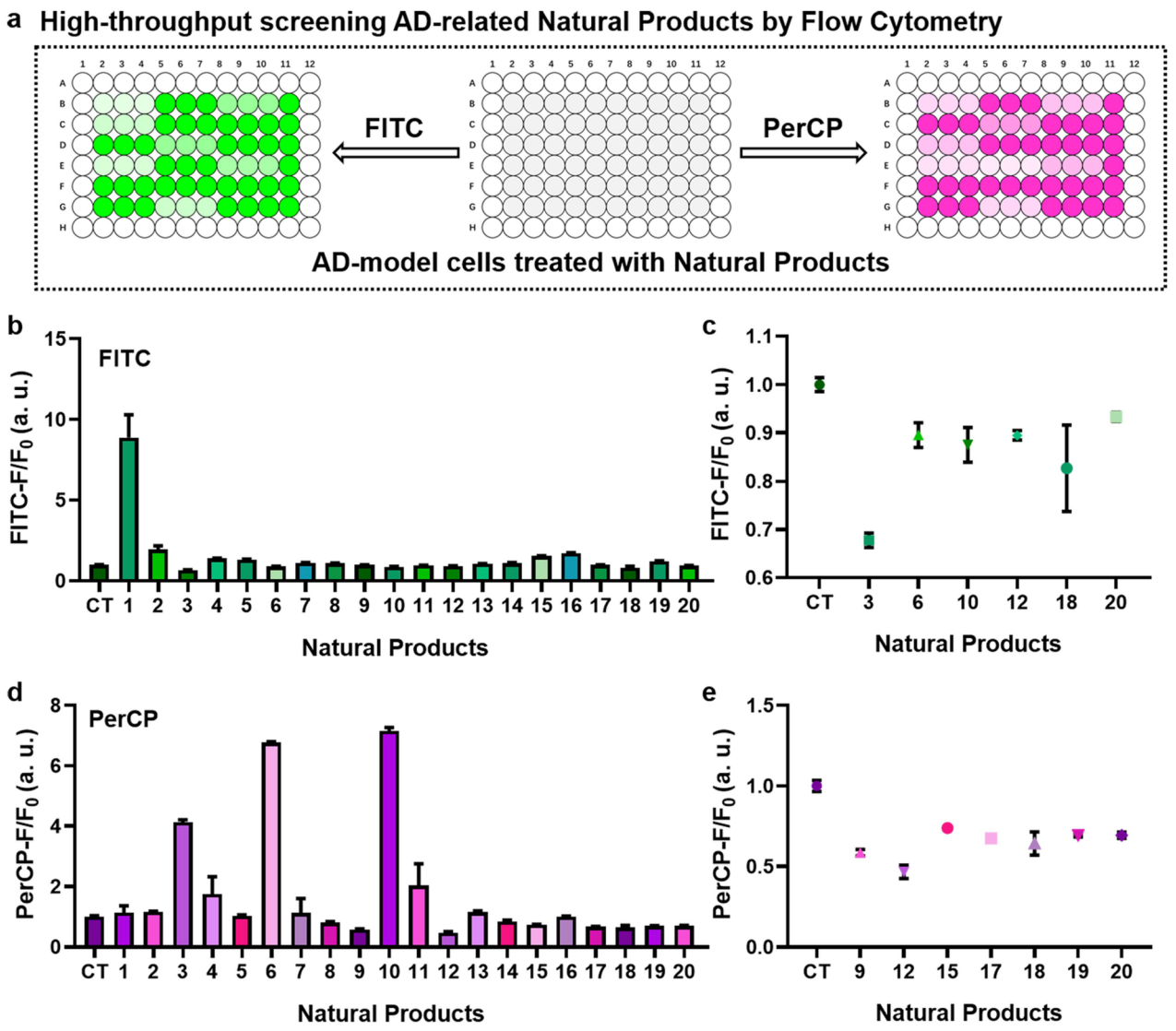

Figure 6. Evaluation of natural products on intracellular MAO-A and LOX activity in Aβ_{42} oligomer-induced SH-SY5Y cells using **MAP-2F** and flow cytometry. (a) Flow cytometric analysis of SH-SY5Y cells pretreated with Aβ_{42} oligomers followed by exposure to various natural compounds, with **MAP-2F** used to simultaneously detect changes in LOX and MAO-A activity. (b, c) FITC channel: used to analyze the change in LOX levels. (d, e) Per CP channel: used to analyze the changes in MAO-A levels. Tested natural products are as follows: (1) coconut oil: CoOil; (2) ginkgo biloba: Egb; (3) ursolic acid; 4. 2,3,5,4′-tetrahydroxy stilbene-2-O-β-D-glucoside; (5) caffeic acid; (6) resveratrol; (7) astragaloside IV; (8) *trans*-cinnamaldehyde; (9) icariin: ICA; (10) triptolide; (11) ginsenoside Rg1; (12) corni fructus; (13) tea polyphenols; (14) crocin; (15) curcumin; (16) artemisinin; (17) geniposidic acid; (18) forsythoside B; (19) tanshinone IIA; (20) stigmasterol.

indicating compensatory crosstalk between these two enzymes. Further literature review revealed that the mechanisms of action of these compounds are closely linked to Aβ pathology. For example, ursolic acid, curcumin, stigmasterol, forsythoside B, and cornuside attenuated Aβ-induced cytotoxicity; resveratrol enhanced Aβ clearance; and ICA, tanshinone IIA, geniposidic acid, and triptolide inhibited Aβ production.[52−66] These findings further confirmed the correlation between intracellular Aβ load and abnormal MAO-A/LOX expression, reinforcing their role as dual biomarkers and therapeutic targets for AD. Collectively, the integration of **MAP-2F** with flow cytometry offers a robust, sensitive platform for high-throughput screening of modulators targeting MAO-A and LOX. The unique spectral response of **MAP-2F** allows for simultaneous, interference-free detection of both enzymes, enabling rapid evaluation of potential modulators in complex cellular models of AD.

CONCLUSIONS

In summary, we have rationally designed and synthesized a series of dicyanoisophorone-based fluorescent probes, **MAP-X** (X = 2F, 2Cl, 2Br, F, Cl, Br), among which **MAP-2F**, with a 3,5-difluoro substitution, exhibited excellent performance in the selective detection of MAO-A and LOX through different fluorescence emission channels and independent recognition mechanisms. Notably, **MAP-2F** enabled the simultaneous, spatially resolved imaging of endogenous MAO-A and LOX within living neuronal cells, enabling dual-target visualization without overlapping fluorescent signals for the first time. Utilizing this capability, we applied **MAP-2F** to dynamically monitor the enzyme activity status under AD-related pathological stimuli, including Aβ_{42} oligomer, Aβ_{42} aggregate, and Glu treatment, revealing a potential feed-forward mechanism whereby upregulation of LOX promotes the polymerization of Aβ_{42} monomers, which in turn exacerbates

https://doi.org/10.1021/cbmi.5c00102
Chem. Biomed. Imaging XXXX, XXX, XXX−XXX

the expression of MAO-A and LOX. These findings suggest that a pathologic amplification cycle contributes to the development of AD. To further explore the potential for its application, we integrated **MAP-2F** into a high-throughput screening platform for evaluating the MAO-A and LOX regulatory activities across a panel of 20 natural products with reported anti-AD properties. Several Aβ-interacting natural products (ICA, curcumin, geniposidic acid, forsythoside B, tanshinone IIA, stigmasterol, ursolic acid, resveratrol, triptolide, and corni fructus) were identified as effective MAO-A/LOX inhibitors, which is consistent with their known interactions with Aβ pathology. Interestingly, we found dual-inhibitory activities of forsythoside B and stigmasterol, further confirming the dual readout capacity of **MAP-2F**. Overall, this work established **MAP-2F** as a powerful molecular tool for real-time, multiplexed imaging of MAO-A and LOX activity in neurodegenerative disease models, enabling simultaneous screening of pharmacologically active modulators. While the probe demonstrates exceptional potential for cellular imaging—particularly through its NIR emission (660 nm) and low cytotoxicity—its translation to in vivo applications requires further optimization to address challenges in BBB penetration and metabolic stability. Future studies will (i) engineer derivatives with enhanced brain delivery (e.g., lipid-soluble modifications or BBB-targeting moieties) and (ii) validate their performance in AD animal models. Beyond direct biological applications, this study provides a conceptual and methodological framework for designing next-generation fluorescent probes capable of concurrent monitoring of disease-associated enzyme networks. Critically, it offers mechanistic insights into the feed-forward relationship between MAO-A/LOX dysregulation and Aβ-mediated neurotoxicity, opening new avenues for therapeutic target discovery and intervention strategies in Alzheimer's disease.

■ ASSOCIATED CONTENT

Supporting Information

The Supporting Information is available free of charge at https://pubs.acs.org/doi/10.1021/cbmi.5c00102.

Additional experimental details, materials, methods, and additional figures (PDF)

■ AUTHOR INFORMATION

Corresponding Authors

Wei Wei − *State Key Laboratory of Pharmaceutical Biotechnology, School of Life Sciences, Nanjing University, 210023 Nanjing, China;* orcid.org/0000-0003-0845-0527; Email: weiwei@nju.edu.cn

Ling Zhang − *Jiangsu Key Laboratory of New Drug Research and Clinical Pharmacy, School of Pharmacy, Public Experimental Research Center, Xuzhou Medical University, Xuzhou 221002, China;* orcid.org/0000-0001-8140-5840; Email: zhamgling1999@163.com

Jing Zhao − *State Key Laboratory of Coordination Chemistry, Chemistry and Biomedicine Innovation Center (ChemBIC), School of Chemistry and Chemical Engineering, Nanjing University, Nanjing 210023, China;* orcid.org/0000-0001-5177-5699; Email: jingzhao@nju.edu.cn

Yong Qian − *State Key Laboratory of Microbial Technology, Jiangsu Collaborative Innovation Center of Biomedical Functional Materials, School of Chemistry and Materials Science, Nanjing Normal University, Nanjing 210023, China;* orcid.org/0000-0003-3788-3575; Email: yongqian@njnu.edu.cn

Authors

Yanyan Chen − *School of Basic Medical Sciences, Hubei University of Medicine, Shiyan, Hubei 442000, China; State Key Laboratory of Coordination Chemistry, Chemistry and Biomedicine Innovation Center (ChemBIC), School of Chemistry and Chemical Engineering, Nanjing University, Nanjing 210023, China*

Xiuxiu Wang − *State Key Laboratory of Pharmaceutical Biotechnology, School of Life Sciences, Nanjing University, 210023 Nanjing, China*

Complete contact information is available at: https://pubs.acs.org/10.1021/cbmi.5c00102

Author Contributions

Y.Q., J.Z., and Y.C. conceived the project; Y.C. performed the measurements; Y.C. conducted the experiments; Y.Q., J.Z., and Y.C. wrote the paper; J.Z., L.Z., W.W., and X.W. supervised the project. All authors discussed the results and commented on the manuscript.

Notes

The authors declare no competing financial interest.

■ ACKNOWLEDGMENTS

This work was supported by the National Natural Science Foundation of China (22025701, 22293052, 22207053, 22177048, 22477061, and 22074065), the National Science Fund for Excellent Young Scholars (22222704), the Natural Science Foundation of Jiangsu Province (BK20232020 and BK20220764), Nanjing Science and Technology Program (202305003), the Jiangsu Provincial Science and Technology Plan Special Fund (BM2023008), and the National Key R&D Program of China (2023YFA1508900).

■ REFERENCES

(1) Jian, C.; Yan, J.; Zhang, H.; Zhu, J. Recent Advances of Small Molecule Fluorescent Probes for Distinguishing Monoamine Oxidase-a and Monoamine Oxidase-B in Vitro and in Vivo. *Mol. Cell. Probes* **2021**, *55*, No. 101686.

(2) Holt, A.; Berry, M. D.; Boulton, A. A. On the Binding of Monoamine Oxidase Inhibitors to Some Sites Distinct from the Mao Active Site, and Effects Thereby Elicited. *Neurotoxicology* **2004**, *25* (1−2), 251−266.

(3) Maynard, L. S.; Schenker, V. J. Monoamine Oxidase Inhibition by Ethanol in Vitro. *Nature* **1962**, *196* (4854), 575−576.

(4) Collins, G. G. S.; Sandler, M.; Williams, E. D.; Youdim, M. B. H. Multiple Forms of Human Brain Mitochondrial Monoamine Oxidase. *Nature* **1970**, *225* (5235), 817−820.

(5) Shih, J. C.; Ridd, M. J. Monoamine Oxidase: From Genes to Behavior. *Annu. Rev. Neurosci.* **1999**, *22* (1), 197−217.

(6) Nelson, R. J.; Trainor, B. C. Neural Mechanisms of Aggression. *Nat. Rev. Neurosci.* **2007**, *8* (7), 536−546.

(7) Graves, S. M.; Xie, Z.; Stout, K. A.; Zampese, E.; Burbulla, L. F.; Shih, J. C.; Kondapalli, J.; Patriarchi, T.; Tian, L.; Brichta, L.; et al. Dopamine Metabolism by a Monoamine Oxidase Mitochondrial Shuttle Activates the Electron Transport Chain. *Nat. Neurosci* **2020**, *23* (1), 15−20.

(8) Tong, J.; Rathitharan, G.; Meyer, J. H.; Furukawa, Y.; Ang, L. C.; Boileau, I.; Guttman, M.; Hornykiewicz, O.; Kish, S. J. Brain Monoamine Oxidase B and a in Human Parkinsonian Dopamine Deficiency Disorders. *Brain* **2017**, *140* (9), 2460−2474.

(9) Youdim, M. B.; Riederer, P. The Relevance of Glial Monoamine Oxidase-B and Polyamines to the Action of Selegiline in Parkinson's Disease. *Mov. Disord.* **1993**, *8* (Suppl 1), S8−13.
(10) Cai, Z. Monoamine Oxidase Inhibitors: Promising Therapeutic Agents for Alzheimer's Disease (Review). *Mol. Med. Rep* **2014**, *9* (5), 1533−1541.
(11) Damijan Knez, M. S.; Urban Košak; Stanislav Gobec. Dual Inhibitors of Cholinesterases and Monoamine Oxidases for Alzheimer's Disease. *Future Med. Chem.* **2017**, *9* (8), 811−832.
(12) Thomas, T. Monoamine Oxidase-B Inhibitors in the Treatment of Alzheimers Disease. *Neurobiol. Aging* **2000**, *21* (2), 343−348.
(13) Quartey, M. O.; Nyarko, J. N. K.; Pennington, P. R.; Heistad, R. M.; Klassen, P. C.; Baker, G. B.; Mousseau, D. D. Alzheimer Disease and Selected Risk Factors Disrupt a Co-Regulation of Monoamine Oxidase-a/B in the Hippocampus, but Not in the Cortex. *Front. Neurosci.* **2018**, *12*, 419−436.
(14) Jun, Y. W.; Cho, S. W.; Jung, J.; Huh, Y.; Kim, Y.; Kim, D.; Ahn, K. H. Frontiers in Probing Alzheimer's Disease Biomarkers with Fluorescent Small Molecules. *ACS Cent. Sci.* **2019**, *5* (2), 209−217.
(15) Behl, T.; Kaur, D.; Sehgal, A.; Singh, S.; Sharma, N.; Zengin, G.; Andronie-Cioara, F. L.; Toma, M. M.; Bungau, S.; Bumbu, A. G.Role of Monoamine Oxidase Activity in Alzheimer's Disease: An Insight into the Therapeutic Potential of Inhibitors. *Molecules***2021**, *26* (12).3724
(16) Rahman, M. S.; Uddin, M. S.; Rahman, M. A.; Samsuzzaman, M.; Behl, T.; Hafeez, A.; Perveen, A.; Barreto, G. E.; Ashraf, G. M. Exploring the Role of Monoamine Oxidase Activity in Aging and Alzheimer's Disease. *Curr. Pharm. Des.* **2021**, *27* (38), 4017−4029.
(17) Syed, A. U.; Liang, C.; Patel, K. K.; Mondal, R.; Kamalia, V. M.; Moran, T. R.; Ahmed, S. T.; Mukherjee, J. Comparison of Monoamine Oxidase-a, Abeta Plaques, Tau, and Translocator Protein Levels in Postmortem Human Alzheimer's Disease Brain. *Int. J. Mol. Sci.* **2023**, *24* (13), 10808−10826.
(18) Rodriguez, C.; Martinez-Gonzalez, J.; Raposo, B.; Alcudia, J. F.; Guadall, A.; Badimon, L. Regulation of Lysyl Oxidase in Vascular Cells: Lysyl Oxidase as a New Player in Cardiovascular Diseases. *Cardiovasc. Res.* **2008**, *79* (1), 7−13.
(19) Papadantonakis, N.; Matsuura, S.; Ravid, K. Megakaryocyte Pathology and Bone Marrow Fibrosis: The Lysyl Oxidase Connection. *Blood* **2012**, *120* (9), 1774−1781.
(20) Cox, T. R.; Rumney, R. M. H.; Schoof, E. M.; Perryman, L.; Hoye, A. M.; Agrawal, A.; Bird, D.; Latif, N. A.; Forrest, H.; Evans, H. R.; et al. The Hypoxic Cancer Secretome Induces Pre-Metastatic Bone Lesions through Lysyl Oxidase. *Nature* **2015**, *522* (7554), 106−110.
(21) Matsuura, S.; Mi, R.; Koupenova, M.; Eliades, A.; Patterson, S.; Toselli, P.; Thon, J.; Italiano, J. E., Jr.; Trackman, P. C.; Papadantonakis, N.et al.Lysyl Oxidase Is Associated with Increased Thrombosis and Platelet Reactivity. *Blood***2016**, *127* (11), 1493−1501.
(22) Chitty, J. L.; Yam, M.; Perryman, L.; Parker, A. L.; Skhinas, J. N.; Setargew, Y. F. I.; Mok, E. T. Y.; Tran, E.; Grant, R. D.; Latham, S. L.; et al. A First-in-Class Pan-Lysyl Oxidase Inhibitor Impairs Stromal Remodeling and Enhances Gemcitabine Response and Survival in Pancreatic Cancer. *Nat. Cancer* **2023**, *4* (9), 1326−1344.
(23) Byers, P. H.; Siegel, R. C.; Holbrook, K. A.; Narayanan, A. S.; Bornstein, P.; Hall, J. G. X-Linked Cutis Laxa. *N. Engl. J. Med.* **1980**, *303* (2), 61−65.
(24) Aronoff, M. R.; Hiebert, P.; Hentzen, N. B.; Werner, S.; Wennemers, H. Imaging and Targeting Lox-Mediated Tissue Remodeling with a Reactive Collagen Peptide. *Nat. Chem. Biol.* **2021**, *17* (8), 865−871.
(25) Chaudhari, N.; Findlay, A. D.; Stevenson, A. W.; Clemons, T. D.; Yao, Y.; Joshi, A.; Sayyar, S.; Wallace, G.; Rea, S.; Toshniwal, P.; et al. Topical Application of an Irreversible Small Molecule Inhibitor of Lysyl Oxidases Ameliorates Skin Scarring and Fibrosis. *Nat. Commun.* **2022**, *13* (1), 5555.
(26) Rodriguez, C.; Alcudia, J. F.; Martinez-Gonzalez, J.; Guadall, A.; Raposo, B.; Sanchez-Gomez, S.; Badimon, L. Statins Normalize Vascular Lysyl Oxidase Down-Regulation Induced by Proatherogenic Risk Factors. *Cardiovasc. Res.* **2009**, *83* (3), 595−603.
(27) Aslam, T.; Miele, A.; Chankeshwara, S. V.; Megia-Fernandez, A.; Michels, C.; Akram, A. R.; McDonald, N.; Hirani, N.; Haslett, C.; Bradley, M.; et al. Optical Molecular Imaging of Lysyl Oxidase Activity - Detection of Active Fibrogenesis in Human Lung Tissue. *Chem. Sci.* **2015**, *6* (8), 4946−4953.
(28) Cox, T. R.; Gartland, A.; Erler, J. T. Lysyl Oxidase, a Targetable Secreted Molecule Involved in Cancer Metastasis. *Cancer Res.* **2016**, *76* (2), 188−192.
(29) Tang, H.; Leung, L.; Saturno, G.; Viros, A.; Smith, D.; Di Leva, G.; Morrison, E.; Niculescu-Duvaz, D.; Lopes, F.; Johnson, L.; et al. Lysyl Oxidase Drives Tumour Progression by Trapping Egf Receptors at the Cell Surface. *Nat. Commun.* **2017**, *8*, 14909.
(30) Al-U'datt, D.; Allen, B. G.; Nattel, S. Role of the Lysyl Oxidase Enzyme Family in Cardiac Function and Disease. *Cardiovasc. Res.* **2019**, *115* (13), 1820−1837.
(31) Li, Q.; Li, Q. Q.; Jia, J. N.; Liu, Z. Q.; Zhou, H. H.; Jin, W. L.; Mao, X. Y.Sodium Valproate Protects against Neuronal Ferroptosis in Epilepsy Via Suppressing Lysyl Oxidase. *bioRxiv***2020**, 126227.
(32) Okuyama, M.; Jiang, W.; Javidan, A.; Chen, J. Z.; Howatt, D. A.; Yang, L.; Hamaguchi, M.; Yasugi, T.; Aono, J.; Vazquez-Padron, R. I.; et al. Lysyl Oxidase Inhibition Ablates Sexual Dimorphism of Abdominal Aortic Aneurysm Formation in Mice. *Circulation* **2020**, *142* (20), 1993−1995.
(33) Saatci, O.; Kaymak, A.; Raza, U.; Ersan, P. G.; Akbulut, O.; Banister, C. E.; Sikirzhytski, V.; Tokat, U. M.; Aykut, G.; Ansari, S. A.; et al. Targeting Lysyl Oxidase (Lox) Overcomes Chemotherapy Resistance in Triple Negative Breast Cancer. *Nat. Commun.* **2020**, *11* (1), 2416.
(34) Ye, M.; Song, Y.; Pan, S.; Chu, M.; Wang, Z. W.; Zhu, X. Evolving Roles of Lysyl Oxidase Family in Tumorigenesis and Cancer Therapy. *Pharmacol. Ther.* **2020**, *215*, No. 107633.
(35) Mao, X.; Wang, X.; Jin, M.; Li, Q.; Jia, J.; Li, M.; Zhou, H.; Liu, Z.; Jin, W.; Zhao, Y.; et al. Critical Involvement of Lysyl Oxidase in Seizure-Induced Neuronal Damage through Erk-Alox5-Dependent Ferroptosis and Its Therapeutic Implications. *Acta Pharm. Sin. B* **2022**, *12* (9), 3513−3528.
(36) Park, J.; Kim, J. S.; Yang, G.; Lee, H.; Shim, G.; Lee, J.; Oh, Y. K. Lysyl Oxidase-Responsive Anchoring Nanoparticles for Modulation of the Tumor Immune Microenvironment. *J. Controlled Release* **2023**, *360*, 376−391.
(37) Gilad, G. M.; Kagan, H. M.; Gilad, V. H. Evidence for Increased Lysyl Oxidase, the Extracellular Matrix-Forming Enzyme, in Alzheimer's Disease Brain. *Neurosci. Lett.* **2005**, *376* (3), 210−214.
(38) Wilhelmus, M. M.; Bol, J. G.; van Duinen, S. G.; Drukarch, B. Extracellular Matrix Modulator Lysyl Oxidase Colocalizes with Amyloid-Beta Pathology in Alzheimer's Disease and Hereditary Cerebral Hemorrhage with Amyloidosis-Dutch Type. *Exp. Gerontol.* **2013**, *48* (2), 109−114.
(39) Kelly, L.; Sharp, M. M.; Thomas, I.; Brown, C.; Schrag, M.; Antunes, L. V.; Solopova, E.; Martinez-Gonzalez, J.; Rodriguez, C.; Carare, R. O. Targeting Lysyl-Oxidase (Lox) May Facilitate Intramural Periarterial Drainage for the Treatment of Alzheimer's Disease. *Cereb. Circ. Cogn. Behav.* **2023**, *5*, 100171−100179.
(40) Ventura-Antunes, L.; Nackenoff, A.; Romero-Fernandez, W.; Bosworth, A. M.; Prusky, A.; Wang, E.; Carvajal-Tapia, C.; Shostak, A.; Harmsen, H.; Mobley, B.et al.Arteriolar Degeneration and Stiffness in Cerebral Amyloid Angiopathy Are Linked to B-Amyloid Deposition and Lysyl Oxidase. *bioRxiv***2024**, *03* (08), 583563.
(41) Naoi, M.; Maruyama, W.; Akao, Y.; Yi, H.; Yamaoka, Y. Involvement of Type a Monoamine Oxidase in Neurodegeneration: Regulation of Mitochondrial Signaling Leading to Cell Death or Neuroprotection. *J. Neural Transm. Suppl.* **2006**, *71*, 67−77.
(42) Fang, H.; Zhang, H.; Li, L.; Ni, Y.; Shi, R.; Li, Z.; Yang, X.; Ma, B.; Zhang, C.; Wu, Q.; et al. Rational Design of a Two-Photon Fluorogenic Probe for Visualizing Monoamine Oxidase a Activity in Human Glioma Tissues. *Angew. Chem., Int. Ed. Engl.* **2020**, *59* (19), 7536−7541.

https://doi.org/10.1021/cbmi.5c00102
Chem. Biomed. Imaging XXXX, XXX, XXX−XXX

(43) Knoll, J. The Possible Mechanisms of Action of (−)Deprenyl in Parkinson's Disease. *J. Neural Transmission* **1978**, *43*, 177−198.
(44) Lee, H. T.; Choi, M. R.; Doh, M. S.; Jung, K. H.; Chai, Y. G. Effects of the Monoamine Oxidase Inhibitors Pargyline and Tranylcypromine on Cellular Proliferation in Human Prostate Cancer Cells. *Oncol. Rep.* **2013**, *30* (4), 1587−1592.
(45) Shang, J.; Shi, W.; Li, X.; Ma, H. Water-Soluble near-Infrared Fluorescent Probes for Specific Detection of Monoamine Oxidase a in Living Biosystems. *Anal. Chem.* **2021**, *93* (9), 4285−4290.
(46) Li, X.; Shi, D.; Song, Y.; Xu, Y.; Gao, Y.; Qiu, W.; Chen, X.; Li, X.; Huang, Y.; Feng, Y.; et al. Specific Tracking of Monoamine Oxidase a in Heart Failure Models by a Far-Red Fluorescent Probe with an Ultra Large Stokes Shift. *Chin. Chem. Lett.* **2022**, *33* (3), 1572−1576.
(47) Shu, Y.; Liu, Y.; Gao, Y.; Li, J. Ph-Triggered Mitochondria Targeting Fluorescent Probe for Detecting Monoamine Oxidases a in Living Cells. *Sens. Actuators B Chem.* **2023**, *390*, No. 133912.
(48) Martinez-Martinez, E.; Rodriguez, C.; Galan, M.; Miana, M.; Jurado-Lopez, R.; Bartolome, M. V.; Luaces, M.; Islas, F.; Martinez-Gonzalez, J.; Lopez-Andres, N.; et al. The Lysyl Oxidase Inhibitor (Beta-Aminopropionitrile) Reduces Leptin Profibrotic Effects and Ameliorates Cardiovascular Remodeling in Diet-Induced Obesity in Rats. *J. Mol. Cell. Cardiol.* **2016**, *92*, 96−104.
(49) Tian, J.; Du, E.; Guo, L. Mitochondrial Interaction with Serotonin in Neurobiology and Its Implication in Alzheimer's Disease. *J. Alzheimers Dis. Rep.* **2023**, *7* (1), 1165−1177.
(50) Cochet, M.; Donneger, R.; Cassier, E.; Gaven, F.; Lichtenthaler, S. F.; Marin, P.; Bockaert, J.; Dumuis, A.; Claeysen, S. 5-Ht4 Receptors Constitutively Promote the Non-Amyloidogenic Pathway of App Cleavage and Interact with Adam10. *ACS Chem. Neurosci.* **2013**, *4* (1), 130−140.
(51) Bar-Am, O.; Amit, T.; Weinreb, O.; Youdim, M. B.; Mandel, S. Propargylamine Containing Compounds as Modulators of Proteolytic Cleavage of Amyloid-Beta Protein Precursor: Involvement of Mapk and Pkc Activation. *J. Alzheimers Dis.* **2010**, *21* (2), 361−371.
(52) Marambaud, P.; Zhao, H.; Davies, P. Resveratrol Promotes Clearance of Alzheimer's Disease Amyloid-Beta Peptides. *J. Biol. Chem.* **2005**, *280* (45), 37377−37382.
(53) Hong, S. Y.; Jeong, W. S.; Jun, M. Protective Effects of the Key Compounds Isolated from Corni Fructus against Beta-Amyloid-Induced Neurotoxicity in Pc12 Cells. *Molecules* **2012**, *17* (9), 10831−10845.
(54) Pasinetti, G. M.; Wang, J.; Ho, L.; Zhao, W.; Dubner, L. Roles of Resveratrol and Other Grape-Derived Polyphenols in Alzheimer's Disease Prevention and Treatment. *Biochim. Biophys. Acta* **2015**, *1852* (6), 1202−1208.
(55) Shi, X.; Zheng, Z.; Li, J.; Xiao, Z.; Qi, W.; Zhang, A.; Wu, Q.; Fang, Y. Curcumin Inhibits Abeta-Induced Microglial Inflammatory Responses in Vitro: Involvement of Erk1/2 and P38 Signaling Pathways. *Neurosci. Lett.* **2015**, *594*, 105−110.
(56) Moussa, C.; Hebron, M.; Huang, X.; Ahn, J.; Rissman, R. A.; Aisen, P. S.; Turner, R. S. Resveratrol Regulates Neuro-Inflammation and Induces Adaptive Immunity in Alzheimer's Disease. *J. Neuroinflammation* **2017**, *14* (1), 1−10.
(57) Reddy, P. H.; Manczak, M.; Yin, X.; Grady, M. C.; Mitchell, A.; Tonk, S.; Kuruva, C. S.; Bhatti, J. S.; Kandimalla, R.; Vijayan, M.; et al. Protective Effects of Indian Spice Curcumin against Amyloid-Beta in Alzheimer's Disease. *J. Alzheimers Dis.* **2018**, *61* (3), 843−866.
(58) Shal, B.; Ding, W.; Ali, H.; Kim, Y. S.; Khan, S. Anti-Neuroinflammatory Potential of Natural Products in Attenuation of Alzheimer's Disease. *Front. Pharmacol.* **2018**, *9*, 548.
(59) Geng, L.; Liu, W.; Chen, Y. Tanshinone Iia Attenuates Abeta-Induced Neurotoxicity by Down-Regulating Cox-2 Expression and Pge2 Synthesis Via Inactivation of Nf-Kappab Pathway in Sh-Sy5y Cells. *J. Biol. Res.* **2019**, *26*, 15.
(60) Lu, X.; Yang, B.; Yu, H.; Hu, X.; Nie, J.; Wan, B.; Zhang, M.; Lu, C. Epigenetic Mechanisms Underlying the Effects of Triptolide and Tripchlorolide on the Expression of Neuroligin-1 in the Hippocampus of App/Ps1 Transgenic Mice. *Pharm. Biol.* **2019**, *57* (1), 453−459.
(61) Yang, W.; Zhang, J.; Shi, L.; Ji, S.; Yang, X.; Zhai, W.; Zong, H.; Qian, Y. Protective Effects of Tanshinone Iia on Sh-Sy5y Cells against Oabeta(1−42)-Induced Apoptosis Due to Prevention of Endoplasmic Reticulum Stress. *Int. J. Biochem. Cell Biol.* **2019**, *107*, 82−91.
(62) Kong, F.; Jiang, X.; Wang, R.; Zhai, S.; Zhang, Y.; Wang, D. Forsythoside B Attenuates Memory Impairment and Neuroinflammation Via Inhibition on Nf-Kappab Signaling in Alzheimer's Disease. *J. Neuroinflammation* **2020**, *17* (1), 305.
(63) Zhang, D. P.; Lu, X. Y.; He, S. C.; Li, W. Y.; Ao, R.; Leung, F. C.; Zhang, Z. M.; Chen, Q. B.; Zhang, S. J. Sodium Tanshinone Iia Sulfonate Protects against Abeta-Induced Cell Toxicity through Regulating Abeta Process. *J. Cell Mol. Med.* **2020**, *24* (6), 3328−3335.
(64) Zhou, Z.; Hou, J.; Mo, Y.; Ren, M.; Yang, G.; Qu, Z.; Hu, Y. Geniposidic Acid Ameliorates Spatial Learning and Memory Deficits and Alleviates Neuroinflammation Via Inhibiting Hmgb-1 and Downregulating Tlr4/2 Signaling Pathway in App/Ps1Mice. *Eur. J. Pharmacol.* **2020**, *869*, No. 172857.
(65) Pratiwi, R.; Nantasenamat, C.; Ruankham, W.; Suwanjang, W.; Prachayasittikul, V.; Prachayasittikul, S.; Phopin, K. Mechanisms and Neuroprotective Activities of Stigmasterol against Oxidative Stress-Induced Neuronal Cell Death Via Sirtuin Family. *Front. Nutr.* **2021**, *8*, No. 648995.
(66) Yang, Z.; Zhou, D. D.; Huang, S. Y.; Fang, A. P.; Li, H. B.; Zhu, H. L. Effects and Mechanisms of Natural Products on Alzheimer's Disease. *Crit. Rev. Food Sci. Nutr.* **2023**, *63* (18), 3168−3188.

https://doi.org/10.1021/cbmi.5c00102
Chem. Biomed. Imaging XXXX, XXX, XXX−XXX